



Controlling secondary flows in Taylor–Couette flow using axially spaced superhydrophobic surfaces

Vignesh Jeganathan¹, Tala Shannak¹, Kamran Alba^{2,†} and Rodolfo Ostilla-Mónico^{1,3,‡}

¹Department of Mechanical Engineering, University of Houston, Houston 77004, USA

²Department of Engineering Technology, University of Houston, Houston 77004, USA

³Departamento de Ingeniería Mecánica y Diseño Industrial, Escuela de Ingeniería, Universidad de Cádiz, 11519 Puerto Real, Spain

(Received 27 September 2022; revised 1 July 2023; accepted 17 July 2023)

Turbulent shear flows are abundant in geophysical and astrophysical systems and in engineering-technology applications. They are often riddled with large-scale secondary flows that drastically modify the characteristics of the primary stream, preventing or enhancing mixing, mass and heat transfer. Using experiments and numerical simulations, we study the possibility of modifying these secondary flows by using superhydrophobic surface treatments that reduce the local shear. We focus on the canonical problem of Taylor–Couette flow, the flow between two coaxial and independently rotating cylinders, which has robust secondary structures called Taylor rolls that persist even at significant levels of turbulence. We generate these structures by rotating only the inner cylinder of the system, and show that an axially spaced superhydrophobic treatment can weaken the rolls through a mismatching surface heterogeneity, as long as the roll size can be fixed. The minimum hydrophobicity of the treatment required for this flow control is rationalized, and its effectiveness beyond the Reynolds numbers studied here is also discussed.

Key words: turbulence control, mixing enhancement, Taylor–Couette flow

1. Introduction

Shear flows are an extremely common occurrence in nature and technology. A simple example would be the fluid motion between two differentially moving parallel plates. More complex examples abound: from wind currents in the atmosphere at different speeds

† Email addresses for correspondence: kalba@central.uh.edu, rodolfo.ostilla@uca.es

(Pedlosky 1987; Newman, Terry & Ware 2007), to flow inside an industrial centrifugal reactor (Schrimpf *et al.* 2021). A primary shear flow field generally involves adjacent fluid layers that move at different speeds. Under certain conditions, the primary flow can be hydrodynamically unstable and any perturbation will lead to a complex three-dimensional flow, where secondary structures can arise that are superimposed on the primary stream (Orszag & Patera 1983). Notable laminar secondary structures are found in the arteries in its curves and branches (Ku *et al.* 1997). On the other hand, turbulent secondary structures are commonly found in geophysical and astrophysical occurrences, such as atmospheric convection cells responsible for the water cycle (Agee 1984; Atkinson & Wu Zhang 1996). They also exist in centrifugal reactors (Schrimpf *et al.* 2021) and rotating reverse osmosis filtration devices (Lee & Lueptow 2001*a,b*).

Secondary flows are a crucial component of the global properties of a system because they account for a major portion of the mass and momentum transport. Hence, the ability to affect or control these secondary structures could lead to affecting global transport properties or even the frictional losses in a system. The scientific interest behind this possibility has led to many attempts at secondary flow control (Qi *et al.* 2012; Bakhuis *et al.* 2018, 2020; Naim & Baig 2019). A natural place to start this investigation is to simplify the flow as much as possible to canonical models. One of the most frequently studied canonical models for shear flows and its secondary structure is Taylor–Couette flow (TCF) and its Taylor rolls, respectively.

Taylor–Couette flow (Donnelly 1991; Grossmann, Lohse & Sun 2016) is the movement of the fluid between two concentric cylinders that rotate independently. A secondary flow called a Taylor roll forms if the flow is centrifugally (or Rayleigh) unstable, i.e. if the angular momentum of the inner cylinder is larger than that of the outer cylinder. At low Reynolds numbers, these are axisymmetric and laminar (Taylor 1923). As the Reynolds number increases, they go through a series of instabilities where they transition to increasingly turbulent states: first to wavy Taylor vortex flow, then to temporally modulated turbulent Taylor rolls and finally to turbulent Taylor rolls (Andereck, Liu & Swinney 1986). As large Reynolds numbers are reached ($Re \sim O(10^5)$), turbulent Taylor rolls wash away in certain regions of parameter space, and where they remain, their main driver is the combination of shear and solid body rotation (Lathrop, Fineberg & Swinney 1992*b*; Huisman *et al.* 2014; Sacco, Verzicco & Ostilla-Mónico 2019).

Taylor rolls are a particularly interesting example of a secondary flow because of their robustness in the turbulent regime (Zhu *et al.* 2016; Ostilla-Mónico *et al.* 2017), and the possibility that multiple stable solutions (‘roll states’ with different roll sizes) can occur for the same boundary conditions (Coles 1965; Huisman *et al.* 2014; Martínez-Arias *et al.* 2014; Wen *et al.* 2020). Furthermore, Taylor rolls are commonly used in engineering applications to affect mixing properties (Lee & Lueptow 2001*a,b*; Schrimpf *et al.* 2021) and represent a large portion of the momentum transport across the cylinder gap (Brauckmann & Eckhardt 2013; Ostilla-Mónico *et al.* 2016*b*). By successfully modifying robust Taylor rolls, we can demonstrate a general capacity to modify secondary flows. The findings here can also be applied directly to TCF or TCF-like systems in engineering, such as centrifugal mixers or bioreactors.

A successful approach to affect turbulent secondary structures is to force an additional secondary flow at a different wavelength from the existing structures. This would generate a mismatch that interferes with existing or ‘natural’ secondary flows and weakens them (Bakhuis *et al.* 2018; Jeganathan, Alba & Ostilla-Mónico 2021). In the current study we will attempt to induce Prandtl secondary flows of the second kind (Nikitin, Popelenskaya & Stroh 2021), which are turbulent secondary flows that arise to compensate for imbalances

(mainly in the mean Reynolds stresses) through turbulent pulsations and can be found, for example, in turbulent rectangular pipes (Hoagland 1962). The advantage of using this method is that this interference can be achieved through selective surface treating without substantially modifying an existing geometry. For example, patterns of heterogeneous roughness induce swirling motions in regions between high- and low-momentum pathways (Nugroho, Hutchins & Monty 2013; Barros & Christensen 2014; Willingham *et al.* 2014; Anderson *et al.* 2015). This swirling motion leads to secondary flows that are generated and sustained due to spanwise gradients in the Reynolds stress components, which cause an imbalance between the production and dissipation of turbulent kinetic energy that necessitates secondary advective velocities to balance (Anderson *et al.* 2015). In a similar spirit, a recent study has showed that heterogeneous axially spaced roughness (equivalent to spanwise roughness in a plane geometry) is a plausible mechanism to control secondary flows in TCF (Bakhuis *et al.* 2020). Through a combined use of experiments and simulations, this study has reported that certain distributions of roughness induce a new, spatially fixed secondary flow that is absent from the base flow, and this effect has resulted in a large change in flow properties.

However, using roughness modifications to affect a system generally results in an increase in overall drag and causes energy losses in real-world applications. An alternative to using roughness, which increases local shear stress, is to attempt to induce the same types of secondary flow by using hydrophobic surfaces, which reduces local stress compared with untreated surfaces. This would induce similar stress imbalances and generate Prandtl secondary flows (Türk *et al.* 2014). Idealized stress-free boundary inhomogeneities in TCF have been simulated in previous studies (Naim & Baig 2019; Jeganathan *et al.* 2021), which have reported a substantial modification of secondary flows when using axial (spanwise) boundary heterogeneity, with the effects persisting up to Reynolds numbers of the order of $Re \sim O(10^4)$. The effects are greatest when the axial heterogeneity is distributed in a pattern with a characteristic wavelength of half the wavelength of the natural structure (a single Taylor roll), causing a weakening interference between the two secondary flows (Jeganathan *et al.* 2021).

A drawback of these numerical studies is that idealized stress-free boundaries are impossible to achieve in engineering applications, thus the potential for real-world applications is uncertain. In this paper we set out to investigate whether this is experimentally feasible, i.e. whether it is possible to control secondary flows using the types of stress-reducing surfaces available in a laboratory setting. To do this, we will use a highly accessible superhydrophobic (SHP) coating (Jeevahan *et al.* 2018) and assess its effects on TCF. Superhydrophobic coatings, unlike the stress-free limits attainable in computer simulations, have a finite-slip length and are often heavily tested for their durability (Xue *et al.* 2015; Wang *et al.* 2016). Recent efforts (Lambley, Schutzius & Poulikakos 2020; Wang *et al.* 2020) show that it is indeed possible to achieve durable SHP surfaces that can withstand extreme conditions, paving the way for studies such as the present one.

The use of SHP surfaces for flow control has not been well explored, especially in the turbulent regime. However, there are some indications that they could be effective, such as reports that SHP surfaces can delay the onset of vortex shedding in flow over a cylinder, and also increase the shedding frequency of the Kármán vortex, causing premature vortex roll up (Muralidhar *et al.* 2011; Kim, Kim & Park 2015). Another study has pointed out the existence of a large number of coherent structures and a change in the vortex shedding pattern in the near wake of an SHP cylinder (Sooraj *et al.* 2020). In addition to affecting secondary structures, the major impact of introducing stress-free or finite-slip boundary conditions is drag reduction. Indeed, our recent TCF simulations in

Jeganathan *et al.* (2021) reported torque reductions of up to 32 % when using (ideal) axial patterns of 50/50 no-slip/stress-free heterogeneity. In the laboratory, drag reduction through the use of SHP surfaces has been achieved in channel flow experiments (Watanabe, Udagawa & Udagawa 1999; Cheng & Giordano 2002; Tretheway & Meinhart 2002; Ou, Perot & Rothstein 2004). Taylor–Couette flow studies also report a maximum drag reduction of up to 80 % using chemically generated SHP surfaces (Srinivasan *et al.* 2015; Hu *et al.* 2017; Rajappan & McKinley 2020), and up to 90 % using stress reduction limits generated by the Leidenfrost effect (Saranadhi *et al.* 2016; Ayan, Entezari & Chini 2019). However, we emphasize that a pure focus on drag reduction is not our main interest because through the application of SHP treatments, we expect to see a reduction in drag in the majority of cases, provided the surface is sufficiently hydrophobic and durable (Daniello, Waterhouse & Rothstein 2009), as seen, for example, in ship hulls (Dong *et al.* 2013; Hwang *et al.* 2017). We focus mainly on how the secondary structures are affected by these surface treatments, while making sure that the possible energy losses do not substantially increase.

To keep the parameter space simple, we apply SHP surface treatments only to the inner cylinder and focus on the resulting flow organization and torque for a TCF system with pure inner cylinder rotation. We study a Reynolds number of the order of $Re \sim O(10^4)$, where the flow is turbulent and the Taylor rolls persist. The parameter space is further restricted to only axial (spanwise) pattern wavelengths that are large enough to have an impact on large-scale structures, rather than small pattern wavelengths that do not have a significant effect on the flow (Jeganathan *et al.* 2021) and are more difficult to construct.

2. Experiments

2.1. Experimental methods

A schematic of the experimental set-up is shown in figure 1(a). The dimensional and dimensionless parameters are consistently denoted with and without a hat symbol, $\hat{\cdot}$, respectively, throughout this paper. The Taylor–Couette experimental set-up is built using an aluminum inner cylinder of radius, $\hat{r}_i = 76.2$ mm, and an acrylic outer cylinder of radius, $\hat{r}_o = 92.1$ mm, leaving a gap width of $\hat{d} = \hat{r}_o - \hat{r}_i = 15.9$ mm. The length of the cylinders is $\hat{l} = 614.7$ mm. The resulting dimensionless geometric parameters are the radius ratio, $\eta = \hat{r}_i/\hat{r}_o = 0.83$, and the aspect ratio, $\Gamma_z = \hat{l}/\hat{d} = 38.7$. The outer cylinder is fixed, and the inner cylinder is rotated at a rotational velocity, $\hat{\omega}_i$, driven by a brushless DC motor (IKA Eurostar 200 mixer). The shear driving strength can be expressed as a Reynolds number of the inner cylinder, $Re_i = \hat{r}_i\hat{\omega}_i\hat{d}/\hat{\nu}$, where $\hat{\nu}$ is the kinematic viscosity of the working fluid.

As shown in figure 1(a), there is a small gap between the inner cylinder and the end caps at the top and bottom. The end caps are stationary, and this would mean a discontinuity in velocity between the inner cylinder and end caps. To minimize torque losses, the system is filled in a way such that the fluid only fills the gap up to the top surface of the inner cylinder. This means that only the space between the inner cylinder and the bottom end cap contains liquid. The gap between the inner cylinder and the cylinder's top cap contains air. With this set-up we estimate that 20–30 % of the measured torque results from the end caps and other system losses.

To achieve the SHP surfaces required to construct TCF experiments, we use a commercial two-step coating called Ultra-Ever Dry, UltraTech International, as used in a previous TCF study by Hu *et al.* (2017). The first step requires spraying a chemical called ‘bottom coat’ followed by the ‘top coat’ in the second step. The bottom coat is

Controlling flows with axially spaced superhydrophobicity

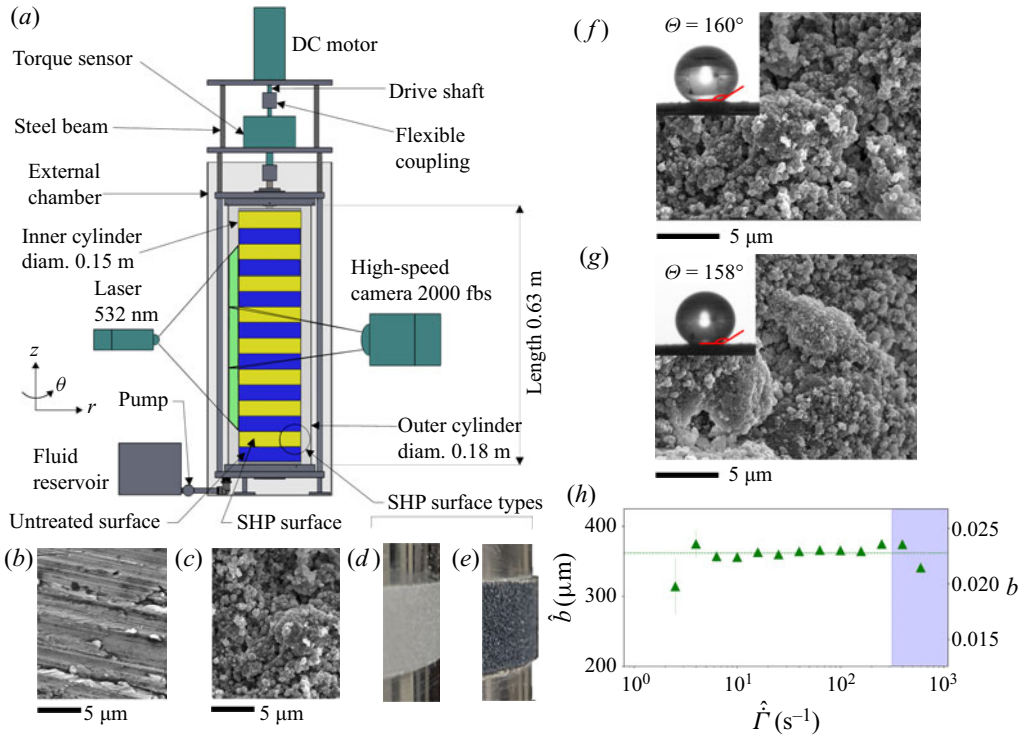


Figure 1. (a) Schematic of experimental set-up. (b,c) Scanning electron microscope images of the untreated aluminum surface (blue region in the schematic) and the SHP surface (yellow region in the schematic), respectively. (d) Flat and (e) stepped SHP modifications on the inner cylinder. Scanning electron microscope images of (f) the freshly coated SHP surface and (g) SHP surface sheared at the highest studied shear rate of $\hat{\Gamma} = 600 \text{ s}^{-1}$ for 90 min. The insets in (f) and (g) depict the contact angle of a $5 \mu\text{L}$ deionized water droplet on the corresponding surfaces. (h) Dimensional slip length (\blacktriangle , green) of the SHP coating measured using the rheometer at various tip shear rates. The right-hand y axis shows the slip length non-dimensionalized by the cylinder gap width, \hat{d} , from the experiments. The dotted green line shows the average slip length $b = 0.023$ of all tip shear rates. The error bars show the average of slip lengths measured during three separate instances (Srinivasan *et al.* 2013). The blue region shows the zone of uncertainty caused by the onset of turbulence in rheometry tests; see [Appendix A](#).

not SHP, but once it cures, it facilitates the self-assembly and bonding characteristic of the microstructures responsible for the superhydrophobicity found in the ‘top coat’. Microscope images comparing the uncoated and SHP surfaces are shown in [figures 1\(b\)](#) and [1\(c\)](#), respectively. We can clearly see that the SHP-treated surface has air-trapping microstructures that cause superhydrophobicity that are largely absent on the uncoated surface. There are two ways by which one may apply the SHP coating on the inner cylinder in TCF experiments. In the first method the treated surfaces are made by sandblasting the inner cylinder, followed by spraying the coatings. This method leaves a nearly flat surface on the inner cylinder as shown in [figure 1\(d\)](#). Therefore, we refer to this treatment as ‘flat SHP’. In the second method we spray the SHP coating on abrasive tapes of 80 grit size, achieving a combined thickness of tape and coating of 0.58 mm . These are fixed on the inner cylinder using an adhesive backing. This leaves a step-like structure on the system as shown in [figure 1\(e\)](#). We accordingly refer to this treatment as ‘stepped SHP’. Superhydrophobic patterns are applied to the inner cylinder in an axially periodic manner,

as shown in [figure 1\(a\)](#). This is achieved by masking portions of the inner cylinder during the coating process.

We define the dimensionless SHP pattern wavelength as $\lambda_z = 2\hat{s}_z/\hat{d}$, with \hat{s}_z being the dimensional axial width of the coating. We will explore three pattern sizes: $\lambda_z = 1.2$, $\lambda_z = 2.4$ and $\lambda_z = 4.8$. We have chosen these three values because of several reasons: (i) they serve to divide the cylinder equally, (ii) they roughly correspond to the values of λ_z studied in Jeganathan *et al.* (2021) (1.17 and 2.33), and (iii) they roughly correspond to one-half, one or twice the Taylor roll wavelength one can expect at these Reynolds numbers. This last point is important as it can serve to experimentally test the prediction from Jeganathan *et al.* (2021), where we found that $\lambda_z = \frac{1}{2}\lambda_{TR}$ was the most effective wavelength in disrupting the turbulent Taylor rolls. We note that with this choice, we cannot distinguish whether $\lambda_z = 1.2$, $\lambda_z = 1.3$ or $\lambda = 1.4$ would be the best fit for this (or any) Taylor–Couette system, but instead focus on giving a proof of concept that axial heterogeneities with wavelengths similar to half the roll size can disrupt turbulent Taylor rolls in an experiment, and that they work better than axial heterogeneities at wavelengths comparable to a single or double roll size. Finally, as mentioned in the introduction, we did not study patterns with wavelengths smaller than $\approx \frac{1}{2}\lambda_{TR}$, as we do not expect them to affect the rolls substantially (Jeganathan *et al.* 2021).

To depict the SHP microstructures more clearly, we show the microscopic image of a freshly coated SHP surface in [figure 1\(f\)](#). These microstructures display superhydrophobicity by creating a low surface energy (Jeevahan *et al.* 2018) and causing the droplet contact angle to be as high as $\Theta = 160^\circ \pm 2^\circ$, as shown in the insert of [figure 1\(f\)](#). To demonstrate the durability of this coating, we present a microscopic image of a water droplet and its contact angle with an SHP surface that has been sheared for 90 min at a shear rate of $\hat{\Gamma} = 600 \text{ s}^{-1}$ in [figure 1\(g\)](#). We use this shear rate and duration as they correspond to the highest Re_i in this study, $Re_i = 2 \times 10^4$, and to the time frame of the TCF experiments. The sheared surface still retains its SHP microstructures and a high contact angle of $\Theta = 158^\circ$, giving us confidence in the ability of the coating to withstand TCF experiments. To study the stress-reducing characteristics of SHP surface, we use the method detailed in Srinivasan *et al.* (2013). The experimental slip length at different tip shear rates $2 \text{ s}^{-1} < \hat{\Gamma} < 600 \text{ s}^{-1}$ is derived from rheometer (HR-3 Discovery hybrid model, TA Instruments) measurements presented in [figure 1\(h\)](#). The average slip length across all the shear rates is found to be $\hat{b} = 360 \pm 12 \text{ }\mu\text{m}$. This corresponds to $b = \hat{b}/\hat{d} = 0.023$ in dimensionless terms. Further details of the characterization of the SHP surface are provided in [Appendices A](#) and [B](#).

Once the SHP surfaces are fixed to the inner cylinders of different axial patterns, we start a series of TCF experiments. The gap between the inner and outer cylinders is filled with deionized water, which is seeded with $50 \text{ }\mu\text{m}$ polyamide seeding particle at 0.2 g L^{-1} to obtain particle image velocity (PIV) data (Buchhave 1992). The working fluid is isolated between the cylinders using various rotary and static rubber seals. Temperature fluctuations are recorded using an Omega HH308 thermometer, revealing that they are within 0.1 K during the PIV experiments. LaVision Nd:YAG laser (532 nm) is used to generate a vertical laser sheet of thickness 2 mm that illuminates the gap between the cylinders. To reduce light refraction errors from the curved acrylic outer cylinder, we have placed the TCF cell inside a cuboidal external chamber. The cuboidal chamber is made from acrylic and filled with water that has a refractive index close to that of acrylic, creating a fish tank (Moisés *et al.* 2016).

The system is started up by accelerating the inner cylinder at 0.279 rad s^{-2} to reach the desired revolutions per minute. For most cases, this achieves a reliable number of rolls, as we detail below. Before starting the PIV measurements, we wait five minutes at a given Re_i so that the flow achieves a statistically stationary state. After this period, we use a high-speed camera (Phantom VEO 710) to record 6000 PIV images (1280×504 pixels) of the fully developed Taylor rolls at 2000 fps for a time period of 3 s. We selected this fps after an extensive parametric study to achieve high-resolution images. The 3 s time period corresponds to ≈ 300 eddy turnover times of Taylor rolls, $\hat{t}_e = \hat{d}/(\hat{r}_i \hat{\omega}_i)$, which is long enough to study their properties, while the initial wait of five minutes corresponds to $\approx 3 \times 10^5$ large-eddy turnover times, more than enough to achieve a statistically stationary state (Ostilla-Mónico *et al.* 2016b). The camera is fitted with a K2 DistaMax long-distance microscope to achieve a 4.4x zoom factor. The PIV images are post processed in MATLAB's open-source PIVlab software (Thielicke & Sonntag 2021) using multi-step interrogation windows ranging from 64×64 to 32×32 pixels. We then obtain the instantaneous radial, \hat{u}_r , and axial, \hat{u}_z , velocity components of the flow. Torque, \hat{T} , is measured for 600 s at a rate of 1000 Hz using an inline rotary ultra-precision torque sensor (Himmelstein MCRT 48801 V[25-0]CFZ). The torque sensor is attached to the driving shaft that connects the motor to the TCF cell. In Appendix C we compare velocity and torque data obtained from our experiment to other experiments and simulations. We use low internal clearance P5 high-precision deep groove SKF ball bearings to reduce the effects of frictional force on the rotary seals, centrifugal forces and the buoyancy of the rotating inner cylinder on the measured torque. The temperature of water is measured during the torque measurement experiments, and the corresponding viscosities and densities are used in the Reynolds number calculations. The density and viscosity of the working fluids at different temperatures are measured using a hand-held density meter (DMA Basic 35) and a rheometer (HR-3 Discovery hybrid model, TA Instruments), respectively.

2.2. Experimental results

To visualize the classic no-slip turbulent TCF, we present the temporally averaged dimensionless radial velocity $\langle u_r \rangle_t$ of the flow field at $Re_i = 10^4$ in figure 2(a) and the corresponding PIV experiment in supplementary movie M1 available at <https://doi.org/10.1017/jfm.2023.606>. The x and y axes are non-dimensionalized by gap width, \hat{d} , with $r = 0$ corresponding to the inner cylinder and $r = 1$ the outer cylinder. The average radial velocity $\langle \hat{u}_r \rangle_t$ is non-dimensionalized using the rotational velocity $\hat{r}_i \hat{\omega}_i$ of the inner cylinder to obtain the dimensionless velocity presented in figure 2. The effect of different wavelengths of the SHP pattern on the turbulent TCF flow field for both flat and stepped patterns is shown in figure 2(b–h) at $Re_i = 10^4$. For the flat patterns, it is apparent that the size of the rolls formed in the system changes across different patterns, something we can attribute to the Taylor–Couette system having a range of possible solutions reflected as changing roll wavelengths (Huisman *et al.* 2014; Martínez-Arias *et al.* 2014). This finding is consistent with Bakhuis *et al.* (2020), who has used axially varying roughness to control a TCF and has observed different roll sizes in their system.

To set the boundary of a pair of rolls and quantify the roll strength, we first calculate the roll (pair) wavelength λ_{TR} . This is given by twice the roll size determined from the axial autocorrelation of the radial velocity at the mid-gap, and in turn this is given by the (axial) distance to the first local minimum of the autocorrelation (Ostilla-Mónico, Verzicco & Lohse 2015). Figure 3(a) shows how the different treatments affect λ_{TR} , quantifying the

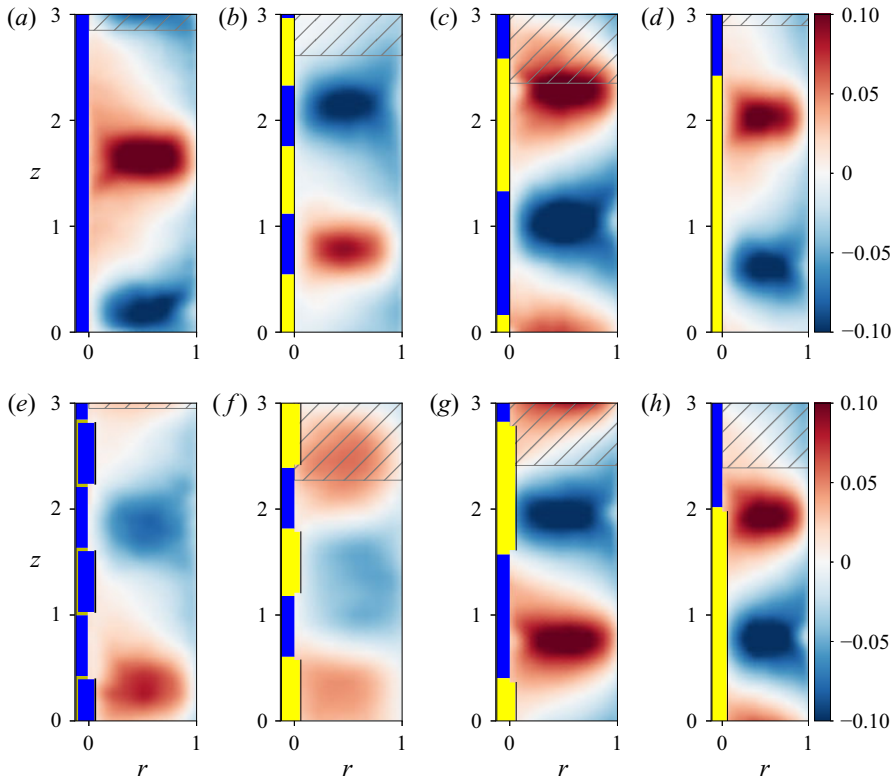


Figure 2. Temporally averaged radial velocity results $\langle u_r \rangle_t$ from experiments at $Re_i = 10^4$. (a–d) No-slip turbulent TCF; flat SHP patterns with wavelengths $\lambda_z = 1.2$, $\lambda_z = 2.4$ and $\lambda_z = 4.8$. (e–h) At $Re_i = 10^4$, stepped pattern with no SHP coating with wavelength $\lambda_z = 1.2$; stepped SHP patterns with wavelengths $\lambda_z = 1.2$, $\lambda_z = 2.4$ and $\lambda_z = 4.8$. The areas striped in grey represent the limits of one roll pair, as measured through the autocorrelation.

previous visual intuition: the roll wavelength λ_{TR} varies by $\pm 20\text{--}30\%$ with respect to the no-slip reference case as the underlying pattern wavelength λ_z is changed.

In addition to the changes in roll size, we can also observe our intended effect: Taylor rolls are slightly affected for $\lambda_z = 1.2$ as seen in figure 2(b), especially when compared with other pattern wavelengths (figures 2c and 2d) and no-slip TCF (figure 2a). To quantify this, we define the roll strength, σ_r , using the standard deviation of the average radial velocity $\langle u_r \rangle_t$ along the axial direction in the mid-gap, $r = 0.5$. We note that this definition is different from what is used, for example, in Sacco *et al.* (2019), where the roll strength is defined using the amplitude of Fourier modes. However, Fourier-based approaches are not suitable for comparisons in this study due to large deviations in the roll shape discussed later. Some care must be taken when comparing σ_r for rolls with a different λ_{TR} , as we can expect different values of σ_r for different sized rolls, as the roll footprint varies as the roll wavelength changes (c.f. Ostilla-Mónico, Lohse & Verzicco (2016a) and Appendix C).

Figure 3(b) shows the roll strength σ_r for all treatments at $Re_i = 10^4$. We first observe that the roll strength corresponding to the pattern wavelength $\lambda_z = 1.2$ is lower than that of the no-slip TCF. The axial signature of the roll is weakened (as shown in figure 2b), and this is reflected as a smaller value of σ_r . The wavelength of this particular SHP pattern is almost equal to the size of a single large-scale structure in the flow (or half

Controlling flows with axially spaced superhydrophobicity

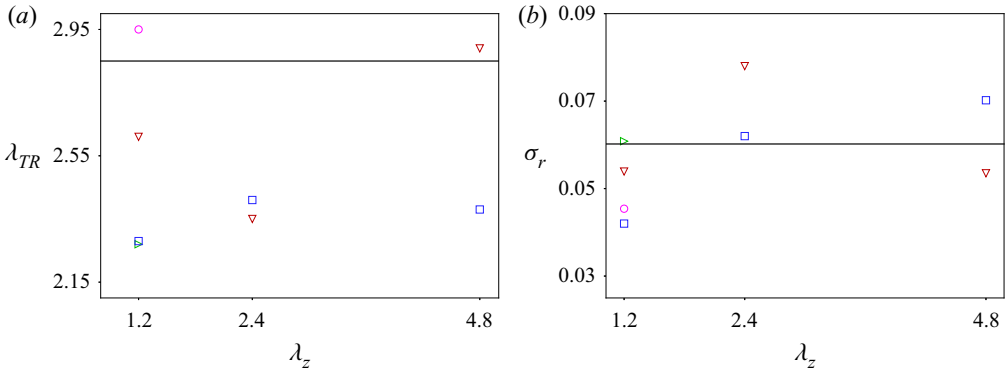


Figure 3. (a) Roll wavelength λ_{TR} obtained from autocorrelations for various flat ∇ (red) and stepped \square (blue) SHP pattern wavelengths at $Re_i = 10^4$. (b) Roll strength σ_r for the same cases. The black horizontal lines represent the reference no-slip roll wavelength $\lambda_{TR} = 2.85$ and roll strength $\sigma_r = 6.02 \times 10^{-2}$, respectively. The \triangleright (green) symbol represents a different roll state obtained for a flat pattern during experiments, and the \circ (magenta) represents the stepped experiment with no treatment.

the roll wavelength). This matches our earlier numerical observations from Jeganathan *et al.* (2021), which also showed dramatic effects on the large-scale structures of TCF when the wavelength of the ideal free-slip pattern is equal to the size of a single structure or half the roll wavelength. Physically, this weakening is caused by the axial heterogeneity, which would generate a secondary flow in a shear flow if none are present (Anderson *et al.* 2015). However, as there already is a secondary flow with a different wavelength, this heterogeneity instead induces a mismatch that interferes with the existing structures, and, as a result, weakens them.

We now turn to the cases with $\lambda_z = 2.4$ and $\lambda_z = 4.8$. Because secondary flows have changed size in response to heterogeneity, as seen in figure 3(a) (∇ , red symbols), the flow statistics will be affected (Ostilla-Mónico *et al.* 2015). Hence, the change in σ_r can potentially be attributed to changes in the roll as well as to the effect of superhydrophobicity (c.f. Appendix C). In the case of $\lambda_z = 2.4$, the value of σ_r is higher than the value for the no-slip case, yet λ_{TR} is also smaller, so no conclusions can be drawn. The case with $\lambda_z = 4.8$ shows a slightly lower value of σ_r than the baseline case, but λ_{TR} is slightly higher, again preventing us from drawing clear conclusions and distinguishing the effect of roll weakening through the SHP treatment from the effects of variation in the roll itself. In summary, while we can see that the treatment with $\lambda = 1.2$ is somewhat effective, as σ_r is lower with a smaller value of λ_{TR} , we cannot point out an optimum flat SHP wavelength as in Jeganathan *et al.* (2021), at which the Taylor rolls could be weakened, or distinguish the effects of different λ_z .

Furthermore, there is the possibility that the system could have roll states with a different number of rolls for the same λ_z . In Taylor–Couette experiments the formation of different roll states is achieved through control of the cylinder acceleration and phase space trajectory (Coles 1965; Huisman *et al.* 2014; Wen *et al.* 2020). In our experiment we do not observe multiplicity of roll states in most cases: with the acceleration profile detailed in the methods section, as well as other acceleration profiles, we reliably obtain a Taylor roll wavelength of $\lambda_{TR} = 2.85$ for the no-slip TCF. On the other hand, for the special case of a $\lambda_z = 1.2$ flat SHP pattern, we can achieve states with different λ_{TR} even when the system was started up with a similar acceleration profile for the cylinders. In figure 3 we have included an additional data point (\triangleright green marker) that denotes another

experimentally accessible state, seen more rarely than the roll state shown in [figure 2\(b\)](#). This state, with a $\lambda_{TR} = 2.27$ wavelength, has a larger value for σ_r when compared with the other experimentally realizable roll state, again showcasing the trend that smaller values of λ_{TR} tend to lead to larger values of σ_r . This means that to fairly assess the treatment, one must fix the roll size, such that the roll modification is not simply a matter of the system finding it easier to access different roll states when the flat SHP pattern is present. Furthermore, to make the treatment weaken the roll in a reproducible manner, one must fix the roll size, which can be a challenging task.

Now, we turn to the stepped SHP patterns. Since the stepped SHP pattern is formed due to a combination of the step feature caused by the abrasive adhesive tape and the SHP coating, it is important to assess whether the steps themselves affect the flow. To show the effect of steps, we have used uncoated smooth filler tape whose thickness is the same height as the stepped SHP surface and pattern wavelength of $\lambda_z = 1.2$ and presented the temporally averaged velocity in [figure 2\(e\)](#) for $Re_i = 10^4$. Although there is some disturbance caused by the steps in the flow, large-scale structures that can be identified as Taylor rolls still remain. The data are represented as \circ (magenta) in [figure 3](#). The roll wavelength is $\lambda_{TR} = 2.95$, very different from the applied λ_z , and larger than the no-slip wavelength. The associated value of σ_r is smaller than that of the no-slip case. However, due to the increased roll wavelength, it cannot be linked to a weakening of the roll.

Having checked this, [figure 2\(f–h\)](#) show the effect of different stepped SHP pattern wavelengths. First, we observe that, unlike flat SHP, the roll size is now fairly constant: $\lambda_{TR} \approx 2.3$ as shown in [figure 3\(a\)](#) (\square , blue symbols), as intended. We hypothesize that the combination of steps with SHP coating reduces the number of possible solutions and helps to fix the roll size. Since the rolls are now comparable across different pattern wavelengths, any observed change in roll strength can be attributed only to the SHP pattern inhomogeneity and not to the size of the formed roll. Furthermore, fixing the roll size increases the chances of affecting them by using precise SHP pattern wavelengths determined by theoretical and numerical methods. The success of this approach is evident from looking at the resulting velocity field for the stepped SHP pattern wavelength of $\lambda_z = 1.2$ in [figure 2\(f\)](#). We again quantify this effect using the roll strength σ_r , and show the results in [figure 3\(b\)](#) (\square , blue symbols). Unlike the flat SHP pattern, we observe a distinct trend of increasing the roll strength with pattern wavelength due to the fixed roll size in the system. We also note the roll strength is the lowest for the stepped SHP $\lambda_z = 1.2$ case, which corresponds to the heavily altered roll state observed in [figure 2\(f\)](#). Therefore, once the roll sizes are fixed, the SHP pattern with $\lambda_z = 1.2$ is revealed to substantially weaken Taylor rolls, which corresponds to the heterogeneity wavelengths of about half the size of the Taylor roll, as in Jeganathan *et al.* (2021). We note that when applying the stepped coating, we reliably obtain the same roll size in the experiments, unlike for the flat treatment, ensuring the reproducibility of the roll modification and that the variations in σ_r can be linked to a roll weakening.

We emphasize that these experiments show that theoretical results can be achieved in a real-world laboratory setting using commercially available treatments. This is further demonstrated by supplementary movie M2. This result should, however, not be taken to mean that *a priori*, $\lambda_z = 1.2$ is better than say 1.3 or 1.4 in disrupting the existing structures, but that treatments with a wavelength equal to approximately half the natural size of the rolls disrupt the rolls better than those with larger wavelengths.

We have checked the effect of increasing Reynolds numbers (and of larger physical shear experiments on our SHP treatment) by extending the analysis to a larger $Re_i = 2 \times 10^4$. We visually show the weakened rolls corresponding to the treatment wavelength of $\lambda_z = 1.2$

Controlling flows with axially spaced superhydrophobicity

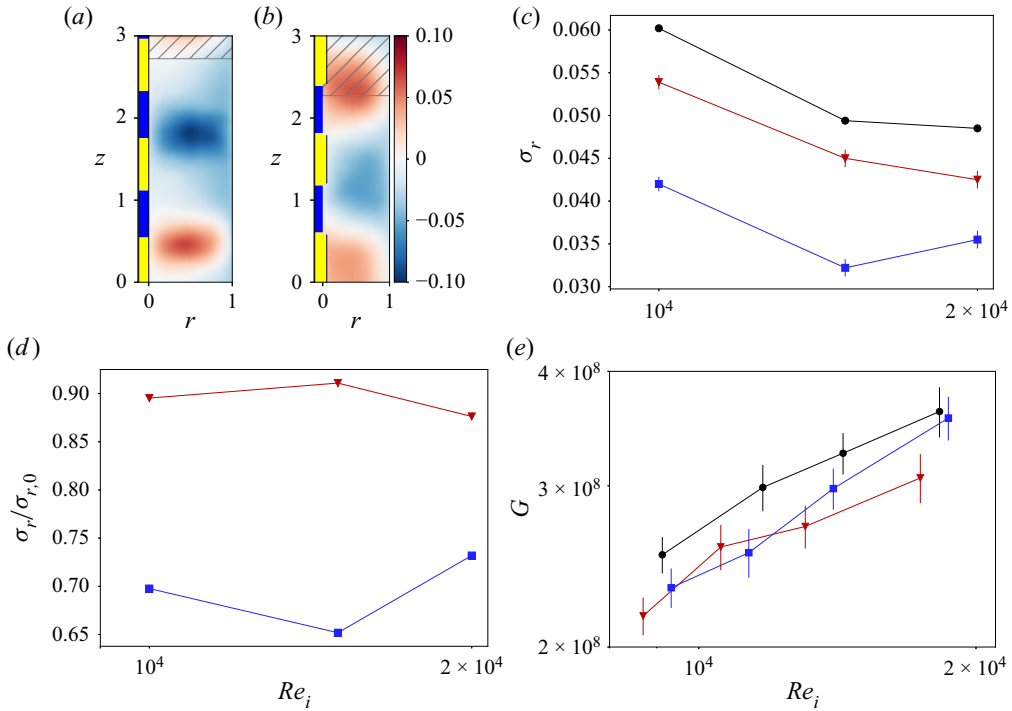


Figure 4. Reynolds number dependence. (a,b) Temporally averaged radial velocity at $Re_i = 2 \times 10^4$ for flat SHP (a) and stepped SHP (b) treatments with $\lambda_z = 1.2$. (c) Roll strength σ_r for no-slip (●, black), $\lambda_z = 1.2$ flat SHP (▼, red) and $\lambda_z = 1.2$ stepped SHP (■, blue) patterns, at different Re_i . (d) Roll strength from treated cases divided by the roll strength for the no-slip reference case. (e) Dimensionless torque G for the same cases. The error bars represent the standard error of the mean of the torque collected from the sensor for 60 000 eddy turnover times, which corresponds to 10 minutes.

for both the flat and stepped SHP patterns at $Re_i = 2 \times 10^4$ in figures 4(a) and 4(b), respectively. The results show a slight change compared with figures 2(b) and 2(f), corresponding to $Re_i = 10^4$. In addition, figure 4(c) shows the roll strength, σ_r , as a function of Re_i for the pattern wavelength of $\lambda_z = 1.2$, providing a comparison between the no-slip TCF (● black line), flat SHP (▼ red line), as well as stepped SHP surface (■ blue line). We clearly see that both the flat and stepped $\lambda_z = 1.2$ SHP patterns make Taylor rolls weaker across all Re_i . As expected, the stepped $\lambda_z = 1.2$ SHP pattern is better at weakening the rolls in the Re_i range studied compared with the flat pattern due to its ability to fix the roll size. This is further corroborated in figure 4(d), which shows the normalized roll strength $\sigma_r/\sigma_{r,0}$, where $\sigma_{r,0}$ is the reference from the no-slip data. It can be appreciated that the flat SHP case only causes a 10% reduction in σ_r , while the stepped case results in a reduction of between 25–35%.

Finally, we compare the effects of the treatment wavelength $\lambda_z = 1.2$ for flat and stepped SHP patterns on torque in figure 4(e). The mean torque is displayed as a dimensionless parameter, $G = \langle \hat{T} \rangle_t / (\hat{\rho} \hat{l} \hat{\nu}^2)$, where $\langle \hat{T} \rangle_t$ is the time average of the discrete torque values, \hat{T} , measured by the torque sensor for 60 000 eddy turnover times (10 min in physical time), here \hat{l} is the length of the inner cylinder, and $\hat{\rho}$ and $\hat{\nu}$ are the density and kinematic viscosity of the working fluid, respectively. The uncertainty in the mean torque is quantified through the standard error of the mean (Gul, Elsinga & Westerweel 2018). The standard error of

the mean is given by $\hat{\epsilon}_T = \hat{\sigma}_T/\sqrt{N}$, where $\hat{\sigma}_T$ is the standard deviation of the torque and N is the number of torque samples collected. For both the flat and stepped SHP patterns, we note that the mean torque on the inner cylinder is lower when compared with the regular no-slip TCF. This is a clear indication of the drag-reduction property of the SHP surfaces. They show relatively similar scaling laws $G \sim Re_i^\alpha$, even if the torque reductions are smaller than those in Jeganathan *et al.* (2021), a point to which we will return below. We also note that the weakening of the rolls, as quantified through σ_r , does not seem to be a good predictor of the torque decrease for the flat SHP case. While this is unlike what was seen in the simulations (Jeganathan *et al.* 2021), we again note that the experiments with flat SHP patterns tend to actually achieve a multiplicity of possible solutions, and this could be causing the erratic increases of G .

3. Direct numerical simulations

3.1. Numerical methods

To further assess the potential applicability of SHP coatings, we have performed a series of direct numerical simulations (DNS) of a similar TCF system using a second-order energy-conserving finite-difference code regularly used in our research group to simulate such systems (van der Poel *et al.* 2015; Jeganathan *et al.* 2021). Direct numerical simulations of TCF are performed in a rotating frame of reference by solving the non-dimensional incompressible Navier–Stokes equations

$$\frac{\partial \mathbf{u}}{\partial t} + \mathbf{u} \cdot \nabla \mathbf{u} + R_\Omega (\mathbf{e}_z \times \mathbf{u}) = -\nabla p + Re_s^{-1} \nabla^2 \mathbf{u}, \quad (3.1)$$

with the incompressibility condition

$$\nabla \cdot \mathbf{u} = 0, \quad (3.2)$$

where \mathbf{u} and p are the non-dimensional velocity and pressure, respectively; t is the non-dimensional time, Re_s is the shear Reynolds number defined below, \mathbf{e}_z is the unit vector in the axial direction and R_Ω is the Coriolis parameter defined below.

The rotating frame is chosen such that the velocities of both cylinders are equal and opposite, $\pm \hat{U}/2$ in dimensional terms. The equations are non-dimensionalized using this velocity \hat{U} and the gap width \hat{d} . This results in two non-dimensional control parameters, the shear Reynolds number $Re_s = \hat{U}\hat{d}/\hat{\nu}$ and the Coriolis parameter $R_\Omega = 2\hat{\Omega}\hat{d}/\hat{U}$, where $\hat{\nu}$ is the kinematic viscosity of the fluid and $\hat{\Omega}$ is the dimensional rotational velocity of the rotating frame.

The domain is taken to be axially periodic, with a periodicity length \hat{L}_z , which can be expressed non-dimensionally as an aspect ratio $\Gamma_z = \hat{L}_z/\hat{d}$. Following Jeganathan *et al.* (2021), the domain is set to be axially periodic with a dimensionless axial periodicity length of $\Gamma_z = \hat{L}_z/\hat{d} = 2.33$. This fixes the wavelength of the roll pair $\lambda_{TR} = \Gamma_z$ and forces the domain to contain a single roll pair. The radius ratio $\eta = \hat{r}_i/\hat{r}_o$ is fixed to $\eta = 0.83$, where \hat{r}_i and \hat{r}_o are the radius of the inner and outer cylinders, corresponding to the experiments. We also impose a rotational symmetry of order $n_{sym} = 10$, corresponding to a streamwise periodicity length of around 2π half-gaps, large enough to obtain asymptotic torque and mean flow statistics (Ostilla-Mónico *et al.* 2015; Jeganathan *et al.* 2021).

Spatial discretization is performed using a second-order energy-conserving centred finite-difference scheme. Time is advanced using a low-storage third-order Runge–Kutta for the explicit terms and a second-order Crank–Nicholson scheme for the implicit

treatment of the wall-normal viscous terms. More details of the algorithm can be found in previous studies Verzicco & Orlandi (1996), van der Poel *et al.* (2015). The code has been heavily validated for the TCF problem (Ostilla-Mónico *et al.* 2014). The spatial resolution used is $n_\theta \times n_r \times n_z = 384 \times 512 \times 768$ in the azimuthal, radial and axial directions, respectively, following Sacco *et al.* (2019).

In a classical TCF problem, the cylinders have a no-slip boundary condition, where the velocity of the fluid at the wall matches the velocity of the cylinder. However, in the present study we alternate no-slip and finite-slip boundary conditions at the wall. Finite-slip boundary conditions are expressed by the combination of (1) a no penetration ($u_r = 0$) and (2) the condition that the two velocity components tangential to the wall equal the slip length times their respective normal derivatives. In non-dimensional terms, this is expressed as $u_\theta = b\partial_r u_\theta$ and $u_z = b\partial_r u_z$. We implement the finite-slip boundary condition by modifying the shear stress τ originating from the wall at the first point on the grid. This is done by modifying the viscous term, which is first approximated using a finite difference of shear stresses ($[\tau^+ - \tau^-]/\Delta r$). Then, these shears are approximated using a finite difference of velocities, u_z or u_θ , depending on the direction being considered. With some rearrangement, this results in a simple correction factor to the geometric factors that multiply the velocity difference. For example, the radial shear stress for u_z at the first grid point is expressed with the following equation:

$$\tau_{z,1}^- = Re_s^{-1} \left. \frac{\partial u_z}{\partial r} \right|_{r_1} = Re_s^{-1} \frac{u_z(r_1) - u_z(r_i)}{r_1 - r_i}. \quad (3.3)$$

Here $u_z(r_i)$ is the axial velocity at the inner cylinder, $u_z(r_1)$ is the axial velocity at the first grid point and r_1 the radial coordinate of the first grid point. In the case of no-slip, $u_z(r_i)$ is equal to the wall velocity (zero for the axial component), while in the case of finite slip, $u_z(r_i)$ is equal to the slip velocity $u_{z,s}$. The slip velocity can be rewritten as $u_{z,s} = b\partial_r u_z(r_1) = bRe_s\tau_{z,1}^-$. Expressed this way, it can be substituted back into (3.3) and the equation is now closed. The finite-difference approach of the code allows us to quickly change between no-slip, finite-slip and free-slip conditions by modifying the metric terms multiplying $\tau_{z,1}^-$, and can allow for potential extensions of this work that consider a spatially or temporally dependent slip length.

The alternating no-slip and finite-slip boundaries applied in the code have a pattern wavelength of $\lambda_z = \lambda_{TR}/2 = 1.17 \approx 1.2$, similar to experiments. We simulate pure inner cylinder rotation with an inner cylinder Reynolds number of $Re_i = 10^4$ to match the experiments by setting $R_\Omega = (1 - \eta) = 0.17$ and $Re_s = 2/(1 + \eta)Re_i = 1.09 \times 10^4$. We then vary the dimensionless slip length, $b = \hat{b}/\hat{d}$, to determine the minimum slip length required for our treatments to be effective in weakening the secondary flows. The simulations are initialized from a zero-velocity condition and, after a transient that usually takes around 200 large-eddy turnover times (\hat{d}/\hat{U}_i), flow statistics are taken for around 600 large-eddy turnover times. This criteria ensures that the time-averaged torque at both cylinders is equal to within 1 %.

3.2. Numerical results

To study the Taylor rolls in the DNS, we average the radial velocity temporally and azimuthally, as opposed to experiments where the PIV data along the azimuth are unavailable. Averaging azimuthally is justified by the statistical homogeneity of TCF, and this allows us to reduce the required running time of the simulations to obtain

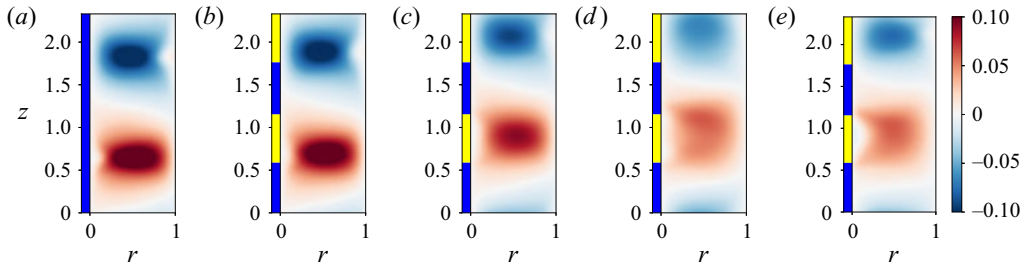


Figure 5. Simulation results. Temporally and azimuthally averaged radial velocity of flat SHP patterns at $Re_i = 10^4$, with pattern wavelength $\lambda_z = 1.2$ and various dimensionless slip lengths $b = \hat{b}/\hat{d}$. (a–e) No slip ($b = 0$), $b = 10^{-4}$, $b = 10^{-2}$, $b = 1$ and free slip ($b \rightarrow \infty$).

adequate statistics. The flow statistics are also averaged in time, as mentioned earlier. We note that a more detailed analysis of the temporal dynamics of turbulent Taylor rolls for fully no-slip cylinders is available in Sacco *et al.* (2019) for the interested reader.

Figure 5 shows the temporally and azimuthally averaged dimensionless radial velocity, $\langle u_r \rangle_{\theta,t}$, for different simulated slip lengths ranging from untreated/no-slip ($b = 0$; figure 5a) to ideal treatment/free-slip ($b \rightarrow \infty$; figure 5e). As expected, Taylor rolls are strongest when there is no treatment. This is also shown in supplementary movie M3. As the slip length increases, the rolls gradually weaken, as seen in figure 5(b–d), with the most effective treatment observed when the surface is fully free slip, as illustrated in figure 5(e) and also in supplementary movie M4. To further quantify this effect, we plot the normalized roll strength $\sigma_r/\sigma_{r,0}$ and the normalized torque G/G_0 against the slip length b in figure 6, respectively. Here, $\sigma_{r,0}$ and G_0 correspond to the roll strength and torque of the untreated no-slip reference case, respectively. The experimental data for the same Re_i and λ_z are also included for completeness. Remarkable agreement is observed for $\sigma_r/\sigma_{r,0}$ between the simulations and the stepped SHP experiment, where the roll size is also fixed. For the torque, both experimental cases show less reduction than the simulation. This can likely be attributed to higher torque losses in the experiments, such as those resulting from axial end caps, which are absent from DNS.

A transition in behaviour, in which treatment begins to be effective, can be observed at $b \approx 3 \times 10^{-3}$. We fit both the roll strength and torque of DNS using a sigmoid function, which are shown in (3.4) and (3.5) (solid green lines in figure 6). The curve fits reads as

$$\frac{\sigma_r}{\sigma_{r,0}} = 1 - \frac{0.362}{1 + \exp\{-1.21(4.684 + \ln b)\}} \quad (3.4)$$

and

$$\frac{G}{G_0} = 1 - \frac{0.3113}{1 + \exp\{-1.135(4.872 + \ln b)\}}. \quad (3.5)$$

As is confirmed by the fits, both curves show an inflection point at $b \approx 10^{-2}$. To better understand why this happens, we must represent the slip length in inner wall units, $b^+ = \hat{b}/\hat{\delta}_v$ (see the upper x axis in both panels of figure 6), where $\delta_v = \hat{v}/\hat{u}_\tau$ is the viscous wall unit, $\hat{u}_\tau = \sqrt{\hat{\tau}_w/\hat{\rho}}$ the frictional velocity and $\hat{\tau}_w$ the averaged shear at the cylinder wall. This (re)normalizes the slip length in terms of the relevant length scales in the boundary layer. In both the normalized roll strength and torque cases of figure 6, we can distinguish three regions of behaviour. In the first region, where the slip length is $b^+ < 1$ ($b < 10^{-3}$), the flow and, hence, the Taylor rolls remain largely unaffected. In this regime

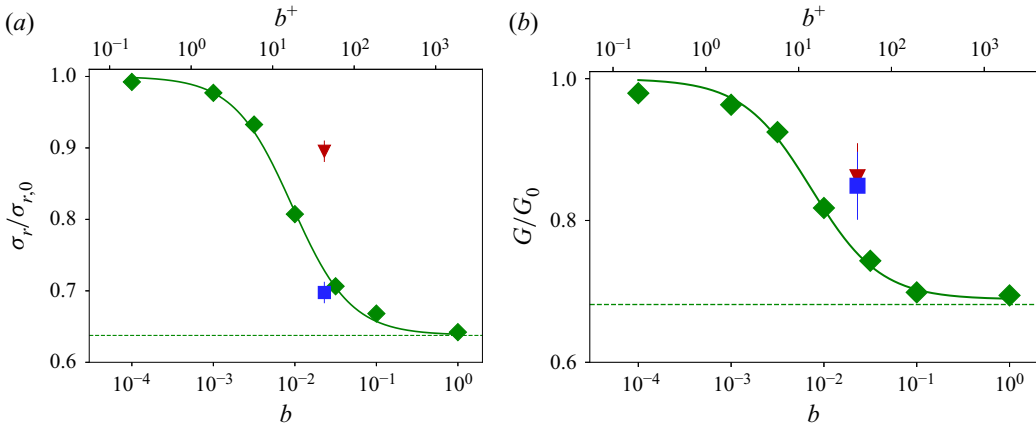


Figure 6. Roll strength σ_r (a) and torque $G(b)$ for SHP $\lambda_z = 1.2$ pattern at $Re_i = 10^4$ for various dimensionless slip lengths b and b^+ (\blacklozenge , green), normalized using the reference no-slip case. Horizontal dashed lines represent the free-slip limit (perfect hydrophobicity). The green curves are the sigmoid fits shown in (3.4) and (3.5). The normalized roll strength and normalized torque of the flat (\blacktriangledown , red) and the stepped (\blacksquare , blue) SHP coated TCF experiments are also shown for $Re_i = 10^4$ and $\lambda_z = 1.2$. The error bars on the right panel represent the standard error of the mean torque collected from the sensor.

the effect of treatment is too weak. The slip length is smaller than the smallest physical scale present in the problem. Hence, it is largely unfelt by the fluid. As the slip length increases, we reach a second region, $1 < b^+ < 100$ ($10^{-3} < b < 10^{-1}$). In this transitional region the treatment is sufficiently effective so that the flow begins to be affected by the boundary inhomogeneity. This, in turn causes the interference effects mentioned above that progressively affect the roll strength and torque. For a treatment to be effective, it has to be strong enough to achieve slip lengths located in this region, where the slip length is comparable to the viscous length scale in the boundary layer. For example, the SHP surface used in the TCF experiments has a slip length $b \approx 0.023$, which is large enough to reach this region and, therefore, can weaken Taylor rolls, as shown by figure 2(f) of the experimental results and DNS presented as supplementary movie M5. In the third region, $b^+ > 100$ ($b > 10^{-1}$), the effect of inhomogeneity reaches a saturation point, where a further increase in slip length does not significantly affect rolls. The treatment behaves as if it were ideal ($b \rightarrow \infty$), as the slip length is now comparable to the largest length scales in the flow. This saturation is reflected in the normalized roll strength and torque that tend toward the asymptotic limit of the free slip, i.e. $b \rightarrow \infty$ or stress free, shown as dashed lines in figure 6.

We can support the claim that the relevant length scale to the treatment's effectiveness is the viscous wall unit by repeating the parameter sweep of b for two additional values of Re_i , i.e. $Re_i = 2 \times 10^4$ and $Re_i = 3 \times 10^4$. In figure 7 we show G/G_0 against b and b^+ for all values of Re_i simulated. When plotted against b , we can clearly see how fitting a sigmoid curve through the data results in a different inflection point, which is smaller for larger Re_i . However, when plotted in terms of b^+ , i.e. when the slip length is non-dimensionalized using $\hat{\delta}_v$, the results collapse much better onto a single curve even if the asymptotic value of $G/G_0(b \rightarrow \infty)$ is different for different Re_i . This supports our hypothesis that the relevant parameter that controls the treatment's effectiveness is b^+ .

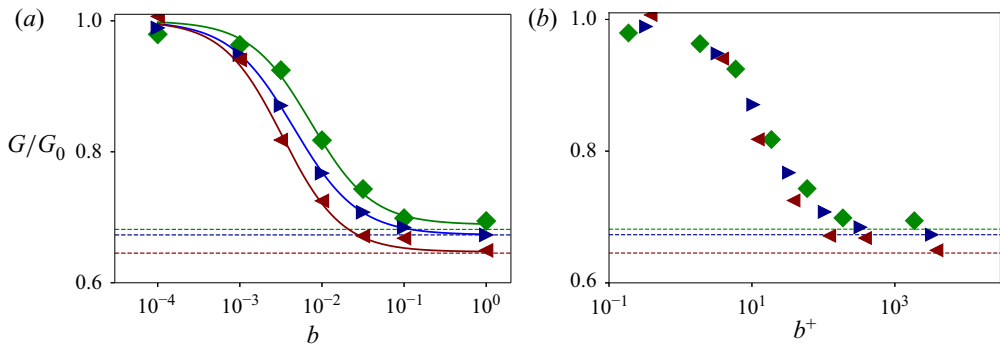


Figure 7. Torque G for SHP $\lambda_z = 1.2$ pattern for various dimensionless slip lengths normalized using the reference no-slip case for $Re_i = 10^4$ (\blacklozenge , green), $Re_i = 2 \times 10^4$ (\blacktriangleright , blue) and $Re_i = 3 \times 10^4$ (\blacktriangleleft , red). (a) The curves are plotted against b the slip length normalized using the gap width, while in (b) they are plotted against b^+ , i.e. the slip length non-dimensionalized using the viscous unit. The horizontal dashed lines represent the free-slip limit (perfect hydrophobicity) for each Reynolds numbers, while the solid curves are sigmoid fits.

4. Summary

To conclude, we state that the ability of SHP coating to weaken the secondary flows depends on the two following key factors.

- (1) As seen in Jeganathan *et al.* (2021), the best treatment pattern depends on the natural length scales of the secondary flow. Although these can be precisely fixed in simulations through the use of small domains, they are often difficult to fix *a priori* in experiments because of the multiple states available to the system. This can drastically reduce the effectiveness of the treatment, as the wavelength mismatch generated by the treatment may not interfere and weaken the existing secondary flow if the length scales do not couple. This has been shown by the difference between flat and stepped SHP surface experiments. Using the flat pattern, we have had difficulty weakening the rolls due to the different roll sizes achieved in the system. However, the stepped SHP pattern has fixed the roll aspect ratio, and we can therefore achieve an SHP pattern that drastically affects Taylor rolls. Special care must be taken to fix the flow length scale, as even changes of 20–30 % in the characteristic length scales of the secondary flow are enough to reduce, or even reverse, the effectiveness of the treatment, as shown in figure 3.
- (2) Another important factor that determines the effectiveness of SHP treatment in turbulent flows is not so much the physical size of the slip length but its dimensionless magnitude in viscous wall units. We have shown that, for a coating to be effective, the dimensionless slip length of the coating should be greater than a viscous wall unit ($b^+ > 1$). This can happen by either having a sufficiently large slip length of the SHP coating or by making the viscous length significantly smaller. This last point leads to the counterintuitive result that SHP treatments should work better at higher Reynolds numbers, as long as they can retain stable air pockets that cause hydrophobicity within its asperities and mechanically survive the imposed shear rates. This last point merits further investigation, as it can open the door to achieving drag reduction and flow control in many types of turbulent wall flows such as pipes or boundary layers by the application of commercially available treatments.

In the more modest context of TCFs, there are other possible and more direct extensions of this work. Firstly, the coatings on the cylinders could be made to have spatially varying

strengths, and this could have a possible effect on the fixing of the roll sizes. This can be done with our current numerical code, but experimentally (and in real-world applications) it presents challenges. One possibility would be to use different hydrophobic coatings. Other potential avenues include modifying the 50/50 split between hydrophobic and untreated surfaces, or treating both cylinders. Finally, another line of research would be using hydrophobic coatings in experimental studies in the linearly stable regime, where the secondary flows arising from the end plates initiate the transition to turbulence (Lopez & Avila 2017). By using these treatments, the effect of end plates could be mitigated.

Supplementary movies. Supplementary movies are available at <https://doi.org/10.1017/jfm.2023.606>.

Acknowledgements. We thank the Research Computing Data Core (RCDC) at the University of Houston for providing computing resources.

Funding. We acknowledge funding from the National Science Foundation through grant NSF-CBET-1934121.

Declaration of interest. The authors report no conflict of interest.

Author ORCIDs.

 Vignesh Jeganathan <https://orcid.org/0000-0002-1663-1240>;

 Kamran Alba <https://orcid.org/0000-0001-9164-3527>;

 Rodolfo Ostilla-Mónico <https://orcid.org/0000-0001-7049-2432>.

Appendix A. Slip length measurement of SHP surfaces using rheometer

To model the solid–liquid interface in macroscopic flows, it is generally assumed that the slip length $\hat{b} = 0$, as it is in the O (nm) range, corresponding to the mean free path of the fluid (Maxwell 1879; Landau & Lifshitz 2013). However, the slip length cannot be neglected while modelling flow over stress-reducing surfaces such as SHP ones whose slip length of O (mm) is much larger than the mean free path of the fluid. Therefore, it becomes imperative to measure the slip length of the SHP surface flows. To do this, we turn to Srinivasan *et al.* (2013), that uses a rheometer to measure the slip length.

A.1. Materials

We use a thin high-precision aluminum square plate of length and width of 8 cm, and a thickness of 0.5 cm as a substrate for the SHP coating. The substrate is sandblasted to obtain a relatively rough surface using #3 glass beads (≈ 0.85 mm diameter). This ensures an adequate grip required to bond the SHP coatings. The SHP treatment (Ultra-Ever Dry, UltraTech International) is applied in two spraying steps. The first step is spraying the chemical called the ‘bottom coat’, followed by 30 min of curing, and finally spraying the ‘top coat’. The bottom coat is not SHP, but it enables bonding and self-assembly of microstructures needed for superhydrophobicity found in the top coat. After 12 h of curing time, the SHP-treated aluminum plate is transferred to a rheometer for slip length measurement.

A.2. Methods

Figure 8(a) shows the schematic of the experimental set-up. The SHP-treated aluminum plate is placed on a temperature-controlled Peltier plate maintained at 21° . A plate geometry of radius $\hat{R} = 20$ mm is attached to a rheometer HR-3 Discovery Hybrid model, TA Instruments, and placed at a distance of $\hat{h} = 1$ mm from the aluminum plate. The gap

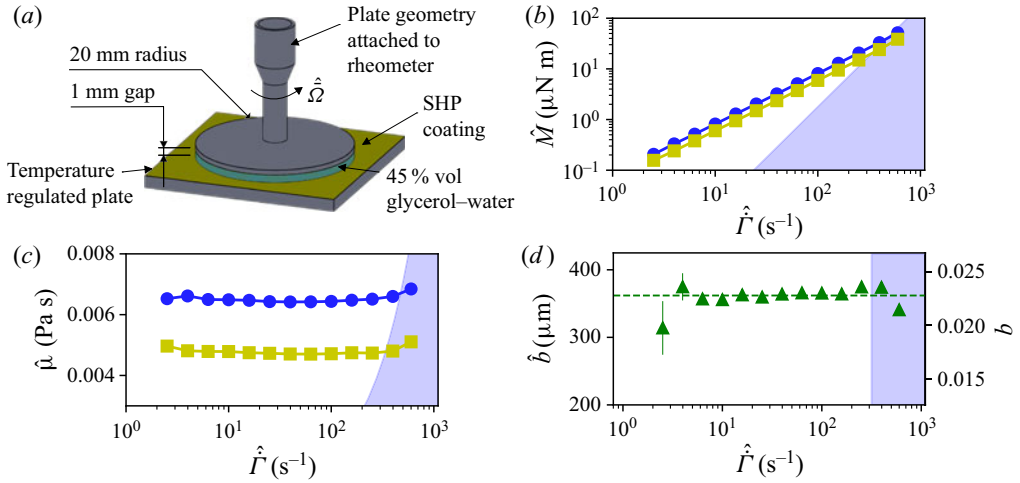


Figure 8. (a) Schematic of the flat plate geometry mounted on a rotational rheometer used to quantify slip length using a 45 % glycerol–water mixture by volume as the probe liquid. (b) Torque measured by the rheometer over the untreated (●, blue) and the SHP surface (■, yellow) at different shear rates. (c) Actual and apparent viscosity of the mixture at different shear rates measured for the untreated and SHP surfaces, respectively. (d) Slip length (▲, green) of the SHP surface measured in μm and non-dimensionalized by the cylinders gap \hat{d} of TCF experiments, at different shear rates (right axis). The dashed green line is the average slip length ($\hat{b} = 360 \mu\text{m}$) calculated across the shear rates (left axis). The error bars show the standard error of mean of slip lengths calculated by repeating the experiment three times. The blue regions show the unreliable zone corresponding to the formation of secondary turbulent flows (Ewoldt, Johnston & Caretta 2015; Mitra *et al.* 2020).

between the SHP surface and the plate geometry is filled with 45 % glycerol–water mixture by volume. Various rotational speeds, $\hat{\Omega}$, corresponding to a tip shear rate $\hat{\Gamma} = \hat{R}\hat{\Omega}/\hat{h}$ in the range of $2 \text{ s}^{-1} < \hat{\Gamma} < 600 \text{ s}^{-1}$ are applied to the enclosed fluid. The resulting torques, \hat{M}_{slip} , and the derived viscosities, $\hat{\mu}_{slip}$, are recorded for 3 min. These are related through the formula (Chhabra & Richardson 2011)

$$\hat{\mu} = \frac{2\hat{M}\hat{h}}{\pi\hat{\Omega}\hat{R}^4} = \frac{2\hat{M}}{\pi\hat{\Gamma}\hat{R}^3}. \quad (\text{A1})$$

Note that the viscosity measured is not the actual viscosity of the fluid but the apparent viscosity caused by the surface modification. To find the actual viscosity, $\hat{\mu}_{no\ slip}$, of the fluid and its corresponding torque, $\hat{M}_{no\ slip}$, the experiment is repeated with a plate that does not have the SHP coating for the same range of shear rate. The slip length, \hat{b} , of the SHP coating is then calculated for each tip shear rate using (A2) (Srinivasan *et al.* 2013):

$$\frac{\hat{M}_{no\ slip}}{\hat{M}_{slip}} = \frac{\hat{\mu}_{no\ slip}}{\hat{\mu}_{slip}} = 1 + \frac{\hat{b}}{\hat{h}}. \quad (\text{A2})$$

The experiment is repeated three times to verify repeatability and to report the standard deviation of the measurements.

A.3. Results

Figure 8(b) shows that the torques obtained using a rheometer for the SHP-coated plate are lower than that of the uncoated plate. This is expected since the SHP coating repels

water, leading to a smaller shear stress compared with that of the uncoated surface. This lower torque also means that the viscosity calculated by the rheometer for the SHP surface is not the actual viscosity of the fluid but an apparent viscosity. This is clearly shown in figure 8(c), where the viscosity calculated from the SHP plate is reduced when compared with the actual viscosity of the working fluid captured by the uncoated plate experiment. Figure 8(d) shows the slip length calculated using (A2), averaged across three repetitions of the same experiment. The average slip length across all the shear rates is found to be $\hat{b} = 360 \pm 12 \mu\text{m}$. This corresponds to $b = \hat{b}/\hat{d} \approx 0.023$ in dimensionless terms, where \hat{d} is the gap width used in the TCF experiments. The blue regions in figure 8(b–d) show the onset of turbulence corresponding to the critical Reynolds number $Re_{crit} \approx 4$ (Ewoldt *et al.* 2015; Mitra *et al.* 2020), where the data are not reliable. The maximum reliable viscosity based on this critical Reynolds number and its corresponding torque that can be measured by the rheometer are given by (A3) and (A4), respectively,

$$\hat{\mu} > \frac{\hat{\rho}\hat{h}^3}{\hat{R}Re_{crit}}\hat{\Gamma}, \tag{A3}$$

$$\hat{M} > \frac{\pi\hat{\rho}\hat{R}^2\hat{h}^3}{2Re_{crit}}\hat{\Gamma}^2. \tag{A4}$$

Here $\hat{\rho}$ in (A3) and (A4) represents the density of the working fluid.

Appendix B. Shear test of SHP samples

Superhydrophobic treatments cause superhydrophobicity on a surface by trapping air in the asperities of a myriad of micro and nanostructures. The durability of the SHP coating hinges on the strength of the bonds that attach these structures to the substrate. When adequate stress is applied, these bonds could be overcome, leading to the removal of microstructures and the loss of superhydrophobicity. This is true especially under extreme conditions such as high pressure-driven channel flows that cause enormous stress on the walls, where the SHP surfaces are largely implemented. Hence, there are a variety of studies (Xue *et al.* 2015; Wang *et al.* 2016) that conduct abrasion studies to assess the durability of coatings. However, these tests are not scenario specific and any conclusion derived from these studies regarding the durability of the SHP coating in our TCF experiments would require substantial approximation. Therefore, we conduct specific shear tests on our SHP coating to study its durability.

B.1. Materials and methods

Eight samples of 1 cm length by 1 cm width are cut using a 0.25 cm thick aluminum plate. The samples are sandblasted and SHP treated using the technique described in the previous section. The samples are fixed on the inner cylinder of the TCF experimental set-up using a double-sided adhesive tape. We fill the gap between the inner and outer cylinders with demineralized water, the same working fluid used to perform all TCF experiments, and shear the samples for $Re_i = 2 \times 10^4$ corresponding to a shear rate of $\hat{\Gamma} = 600 \text{ s}^{-1}$. The samples are subsequently removed at certain intervals, creating a range of specimens, each sheared only for a certain duration. ImageJ (Schneider, Rasband & Eliceiri 2012) is used to measure the contact angles of 5 μL demineralized water droplet snapshots captured with a Phantom VEO 710 camera.

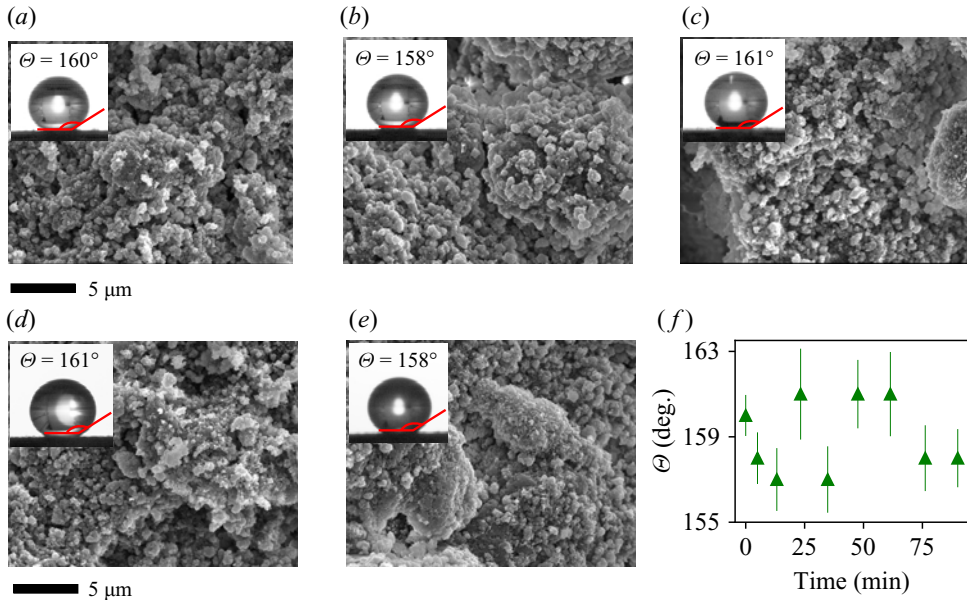


Figure 9. Scanning electron microscope images of the SHP surface under various durations of shear rate $\hat{\Gamma} = 600 \text{ s}^{-1}$: (a) 0 min, (b) 5 min, (c) 20 min, (d) 60 min and (e) 90 min. The insets show the contact angle of a 5 μL demineralized water droplet over the corresponding surfaces. (f) The contact angle (\blacktriangle , green) of SHP surfaces at different durations of shear rate $\hat{\Gamma} = 600 \text{ s}^{-1}$. The error bars show the standard deviation of the contact angle obtained during the elliptical curve fitting of the droplets.

B.2. Results

Figures 9(a)–9(e) show the scanning electron microscope images of the freshly coated SHP sample and those corresponding to various durations of shear rate $\hat{\Gamma} = 600 \text{ s}^{-1}$. It is clear that the SHP coating is durable at the shear rate studied, since all of the samples observed retain microstructures that cause superhydrophobicity. Further proof of superhydrophobicity is seen in the insets of these images, which shows that the contact angle has remained as high as $\Theta = 159^\circ \pm 2^\circ$. The contact angles are plotted against different shear durations of shear rate in figure 9(f).

Appendix C. Torque and velocity benchmarks

In this section we present a series of benchmarks for our experimental set-up. In figure 10 we show uncompensated and compensated torques against Re_i . The data for these measurements is obtained by subtracting the torque measured when the cylinders are filled with water from the torque measured when the cylinders are filled with air. The latter number provides a reference estimate for the losses in the system. We add the benchmark $G = 0.202(\eta^{-1} - 1)^{-5/3} Re_i^{5/3}$ from Marcus (1984), Lathrop, Fineberg & Swinney (1992a). The torque measurements show a degree of dispersion around the benchmark line even though they largely follow the trend.

In figure 11 we compare the velocity data obtained from the PIV performed in experiments to that obtained from simulations. In figure 11(a) we show the experimental results for $\langle u_r \rangle_t$ at the mid-gap in green, as well as the values for $\langle u_r \rangle_{\theta,t}$ obtained from simulations at a similar λ_z in blue. We also show simulation data obtained by only

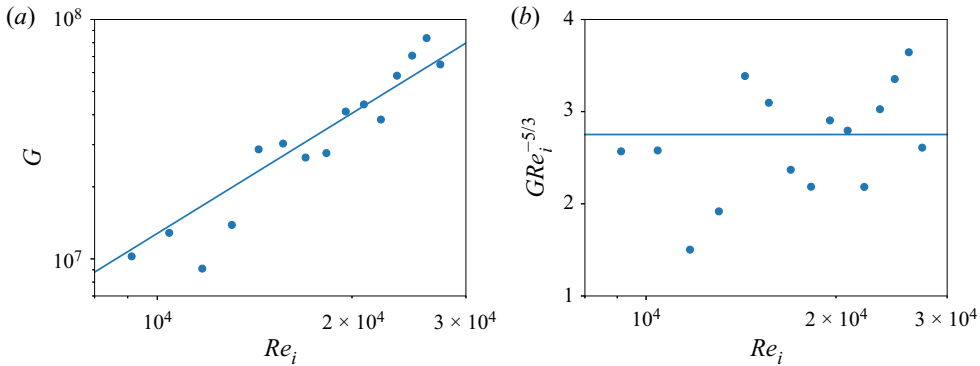


Figure 10. Uncompensated and compensated non-dimensional torque G measurements against Re_i for the untreated cylinders. The solid line is $G = 0.202(\eta^{-1} - 1)^{-5/3} Re_i^{5/3}$ (Marcus 1984; Lathrop *et al.* 1992a).

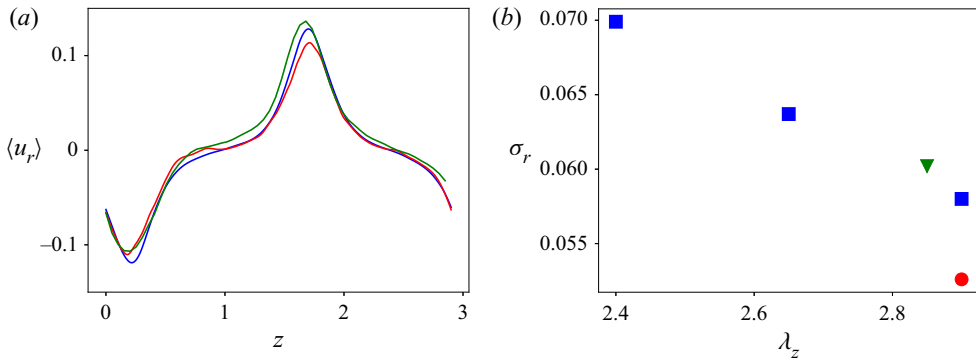


Figure 11. (a) Comparison of the radial velocity at the mid-gap obtained from experiments (green) and simulations (blue for $\langle u_r \rangle_{t,\theta}$, red for $\langle u_r \rangle_t$) for untreated cylinders and $\lambda_z \approx 2.9$. (b) Values of roll strength σ_r obtained from $\langle u_r \rangle_t$ for simulations (●, red) and experiments (▼, green), and from $\langle u_r \rangle_{t,\theta}$ for simulations (■, blue) at $Re_i = 10^4$ for untreated cylinders.

averaging temporally and not azimuthally in red, i.e. $\langle u_r \rangle_t$. We can observe that both procedures for obtaining the average radial velocity in simulations give results that have a similar axial profile as the experiments. The data obtained from simulations by only averaging azimuthally, i.e. $\langle u_r \rangle_t$, appear less statistically converged due to the smaller amount of samples. In figure 11(b) we show the value of σ_r calculated from the no-slip experiment, as well as the value obtained for σ_r from several simulations by using $\langle u_r \rangle_{\theta,t}$ and $\langle u_r \rangle_t$. The numerical procedure for calculating σ_r from $\langle u_r \rangle_{\theta,t}$ results in values of σ_r that match quite well the data obtained from experiments. The value of σ_r obtained from $\langle u_r \rangle_t$ in simulations is slightly lower than the other values. The data also show the trend of σ_r with λ_z described in § 2.2.

REFERENCES

- AGEE, E.M. 1984 Observations from space and thermal convection: a historical perspective. *Bull. Am. Meteorol. Soc.* **65** (9), 938–949.
- ANDERECK, C.D., LIU, S.S. & SWINNEY, H.L. 1986 Flow regimes in a circular Couette system with independently rotating cylinders. *J. Fluid Mech.* **164**, 155–183.

- ANDERSON, W., BARROS, J.M., CHRISTENSEN, K.T. & AWASTHI, A. 2015 Numerical and experimental study of mechanisms responsible for turbulent secondary flows in boundary layer flows over spanwise heterogeneous roughness. *J. Fluid Mech.* **768**, 316–347.
- ATKINSON, B.W. & WU ZHANG, J. 1996 Mesoscale shallow convection in the atmosphere. *Rev. Geophys.* **34** (4), 403–431.
- AYAN, M.S., ENTEZARI, M. & CHINI, S.F. 2019 Experiments on skin friction reduction induced by superhydrophobicity and Leidenfrost phenomena in a Taylor–Couette cell. *Intl J. Heat Mass Transfer* **132**, 271–279.
- BAKHUIS, D., EZETA, R., BERGHOUT, P., BULLEE, P.A., TAI, D., CHUNG, D., VERZICCO, R., LOHSE, D., HUISMAN, S.G. & SUN, C. 2020 Controlling secondary flow in Taylor–Couette turbulence through spanwise-varying-roughness. *J. Fluid Mech.* **883**, 654–662.
- BAKHUIS, D., OSTILLA-MÓNICO, R., VAN DER POEL, E.P., VERZICCO, R. & LOHSE, D. 2018 Mixed insulating and conducting thermal boundary conditions in Rayleigh–Bénard convection. *J. Fluid Mech.* **835**, 491–511.
- BARROS, J.M. & CHRISTENSEN, K.T. 2014 Observations of turbulent secondary flows in a rough-wall boundary layer. *J. Fluid Mech.* **748**, 90–102.
- BRAUCKMANN, H.J. & ECKHARDT, B. 2013 Direct numerical simulations of local and global torque in Taylor–Couette flow up to $Re = 30\,000$. *J. Fluid Mech.* **718**, 398–427.
- BUCHHAVE, P. 1992 Particle image velocimetry—status and trends. *Exp. Therm. Fluid Sci.* **5** (5), 586–604.
- CHENG, J.-T. & GIORDANO, N. 2002 Fluid flow through nanometer-scale channels. *Phys. Rev. E* **65** (3), 031206.
- CHHABRA, R.P. & RICHARDSON, J.F. 2011 *Non-Newtonian Flow and Applied Rheology: Engineering Applications*. Butterworth–Heinemann.
- COLES, D. 1965 Transition in circular couette flow. *J. Fluid Mech.* **21** (3), 385–425.
- DANIELLO, R.J., WATERHOUSE, N.E. & ROTHSTEIN, J.P. 2009 Drag reduction in turbulent flows over superhydrophobic surfaces. *Phys. Fluids* **21** (8), 085103.
- DONG, H., CHENG, M., ZHANG, Y., WEI, H. & SHI, F. 2013 Extraordinary drag-reducing effect of a superhydrophobic coating on a macroscopic model ship at high speed. *J. Mater. Chem. A* **1** (19), 5886–5891.
- DONNELLY, R.J. 1991 Taylor–Couette flow: the early days. *Phys. Today* **44** (11), 32–39.
- EWOLDT, R.H., JOHNSTON, M.T. & CARETTA, L.M. 2015 Experimental challenges of shear rheology: how to avoid bad data. In *Complex Fluids in Biological Systems*, pp. 207–241. Springer.
- GROSSMANN, S., LOHSE, D. & SUN, C. 2016 High–Reynolds number Taylor–Couette turbulence. *Annu. Rev. Fluid Mech.* **48** (1), 53–80.
- GUL, M., ELSINGA, G.E. & WESTERWEEL, J. 2018 Experimental investigation of torque hysteresis behaviour of Taylor–Couette flow. *J. Fluid Mech.* **836**, 635–648.
- HOAGLAND, L.C. 1962 Fully developed turbulent flow in straight rectangular ducts: secondary flow, its cause and effect on the primary flow. PhD thesis, Massachusetts Institute of Technology.
- HU, H., *et al.* 2017 Significant and stable drag reduction with air rings confined by alternated superhydrophobic and hydrophilic strips. *Sci. Adv.* **3** (9), e1603288.
- HUISMAN, S.G., VAN DER VEEN, R.C.A., SUN, C. & LOHSE, D. 2014 Multiple states in highly turbulent Taylor–Couette flow. *Nat. Commun.* **5**, 3820.
- HWANG, G.B., PATIR, A., PAGE, K., LU, Y., ALLAN, E. & PARKIN, I.P. 2017 Buoyancy increase and drag-reduction through a simple superhydrophobic coating. *Nanoscale* **9** (22), 7588–7594.
- JEEVAHAN, J., CHANDRASEKARAN, M., BRITTO JOSEPH, G., DURAIRAJ, R.B. & MAGESHWARAN, G. 2018 Superhydrophobic surfaces: a review on fundamentals, applications, and challenges. *J. Coat. Technol. Res.* **15** (2), 231–250.
- JEGANATHAN, V., ALBA, K. & OSTILLA-MÓNICO, R. 2021 Controlling secondary flows in Taylor–Couette flow using stress-free boundary conditions. *J. Fluid Mech.* **922**, A17.
- KIM, N., KIM, H. & PARK, H. 2015 An experimental study on the effects of rough hydrophobic surfaces on the flow around a circular cylinder. *Phys. Fluids* **27** (8), 085113.
- KU, D.N., *et al.* 1997 Blood flow in arteries. *Annu. Rev. Fluid Mech.* **29** (1), 399–434.
- LAMBLEY, H., SCHUTZIUS, T.M. & POULIKAKOS, D. 2020 Superhydrophobic surfaces for extreme environmental conditions. *Proc. Natl Acad. Sci.* **117** (44), 27188–27194.
- LANDAU, L.D. & LIFSHITZ, E.M. 2013 *Fluid Mechanics: Landau and Lifshitz: Course of Theoretical Physics*, vol. 6. Elsevier.
- LATHROP, D.P., FINEBERG, J. & SWINNEY, H.L. 1992a Transition to shear-driven turbulence in Couette–Taylor flow. *Phys. Rev. A* **46** (10), 6390.
- LATHROP, D.P., FINEBERG, J. & SWINNEY, H.L. 1992b Turbulent flow between concentric rotating cylinders at large Reynolds number. *Phys. Rev. Lett.* **68** (10), 1515–1518.

Controlling flows with axially spaced superhydrophobicity

- LEE, S. & LUEPTOW, R.M. 2001a Reverse osmosis filtration for space mission wastewater: membrane properties and operating conditions. *J. Membr. Sci.* **182** (1-2), 77–90.
- LEE, S. & LUEPTOW, R.M. 2001b Rotating reverse osmosis: a dynamic model for flux and rejection. *J. Membr. Sci.* **192** (1-2), 129–143.
- LOPEZ, J.M. & AVILA, M. 2017 Boundary-layer turbulence in experiments on quasi-keplerian flows. *J. Fluid Mech.* **817**, 21–34.
- MARCUS, P.S. 1984 Simulation of Taylor–Couette flow. Part 1. Numerical methods and comparison with experiment. *J. Fluid Mech.* **146**, 45–64.
- MARTÍNEZ-ARIAS, B., PEIXINHO, J., CRUMEYROLLE, O. & MUTABAZI, I. 2014 Effect of the number of vortices on the torque scaling in Taylor–Couette flow. *J. Fluid Mech.* **748**, 756–767.
- MAXWELL, J.C. 1879 VII. On stresses in rarified gases arising from inequalities of temperature. *Phil. Trans. R. Soc.* **170**, 231–256.
- MITRA, H., JAYARAM, P., BRATSMAN, A., GABEL, T. & ALBA, K. 2020 Characterization and rheology of platelet-rich plasma. *J. Rheol.* **64** (5), 1017–1034.
- MOISÉS, G.V.L., NACCACHE, M.F., ALBA, K. & FRIGAARD, I.A. 2016 Isodense displacement flow of viscoplastic fluids along a pipe. *J. Non-Newtonian Fluid Mech.* **236**, 91–103.
- MURALIDHAR, P., FERRER, N., DANIELLO, R. & ROTHSTEIN, J.P. 2011 Influence of slip on the flow past superhydrophobic circular cylinders. *J. Fluid Mech.* **680**, 459–476.
- NAIM, M.S. & BAIG, M.F. 2019 Turbulent drag reduction in Taylor–Couette flows using different super-hydrophobic surface configurations. *Phys. Fluids* **31** (9), 095108.
- NEWMAN, D.E., TERRY, P.W. & WARE, A.S. 2007 Shear flows and turbulence in nature. *Comput. Sci. Engng* **9** (6), 45–52.
- NIKITIN, N.V., POPELENSKAYA, N.V. & STROH, A. 2021 Prandtl’s secondary flows of the second kind. problems of description, prediction, and simulation. *Fluid Dyn.* **56** (4), 513–538.
- NUGROHO, B., HUTCHINS, N. & MONTY, J.P. 2013 Large-scale spanwise periodicity in a turbulent boundary layer induced by highly ordered and directional surface roughness. *Intl J. Heat Fluid Flow* **41**, 90–102.
- ORSZAG, S.A. & PATERA, A.T. 1983 Secondary instability of wall-bounded shear flows. *J. Fluid Mech.* **128**, 347–385.
- OSTILLA-MÓNICO, R., LOHSE, D. & VERZICCO, R. 2016a Effect of roll number on the statistics of turbulent Taylor–Couette flow. *Phys. Rev. Fluids* **1** (5), 054402.
- OSTILLA-MÓNICO, R., VAN DER POEL, E.P., VERZICCO, R., GROSSMANN, S. & LOHSE, D. 2014 Exploring the phase diagram of fully turbulent Taylor–Couette flow. *J. Fluid Mech.* **761**, 1–26.
- OSTILLA-MÓNICO, R., VERZICCO, R., GROSSMANN, S. & LOHSE, D. 2016b The near-wall region of highly turbulent Taylor–Couette flow. *J. Fluid Mech.* **788**, 95–117.
- OSTILLA-MÓNICO, R., VERZICCO, R. & LOHSE, D. 2015 Effects of the computational domain size on direct numerical simulations of Taylor–Couette turbulence with stationary outer cylinder. *Phys. Fluids* **27** (2), 025110.
- OSTILLA-MÓNICO, R., ZHU, X., SPANDAN, V., VERZICCO, R. & LOHSE, D. 2017 Life stages of wall-bounded decay of Taylor–Couette turbulence. *Phys. Rev. Fluids* **2** (11), 114601.
- OU, J., PEROT, B. & ROTHSTEIN, J.P. 2004 Laminar drag reduction in microchannels using ultrahydrophobic surfaces. *Phys. Fluids* **16** (12), 4635–4643.
- PEDLOSKY, J. 1987 *Geophysical Fluid Dynamics*, vol. 710. Springer.
- VAN DER POEL, E.P., OSTILLA-MÓNICO, R., DONNERS, J. & VERZICCO, R. 2015 A pencil distributed finite difference code for strongly turbulent wall-bounded flows. *Comput. Fluids* **116**, 10–16.
- QI, L., ZOU, Z., WANG, P., CAO, T. & LIU, H. 2012 Control of secondary flow loss in turbine cascade by streamwise vortex. *Comput. Fluids* **54**, 45–55.
- RAJAPPAN, A. & MCKINLEY, G.H. 2020 Cooperative drag reduction in turbulent flows using polymer additives and superhydrophobic walls. *Phys. Rev. Fluids* **5** (11), 114601.
- SACCO, F., VERZICCO, R. & OSTILLA-MÓNICO, R. 2019 Dynamics and evolution of turbulent Taylor rolls. *J. Fluid Mech.* **870**, 970–987.
- SARANADHI, D., CHEN, D., KLEINGARTNER, J.A., SRINIVASAN, S., COHEN, R.E. & MCKINLEY, G.H. 2016 Sustained drag reduction in a turbulent flow using a low-temperature Leidenfrost surface. *Sci. Adv.* **2** (10), e1600686.
- SCHNEIDER, C.A., RASBAND, W.S. & ELICEIRI, K.W. 2012 NIH image to imageJ: 25 years of image analysis. *Nat. Meth.* **9** (7), 671–675.
- SCHRIMPF, M., ESTEBAN, J., WARMELING, H., FÄRBER, T., BEHR, A. & VORHOLT, A.J. 2021 Taylor–Couette reactor: principles, design, and applications. *AIChE J.* **67** (5), e17228.

- SOORAJ, P., RAMAGYA, M.S., KHAN, M.H., SHARMA, A. & AGRAWAL, A. 2020 Effect of superhydrophobicity on the flow past a circular cylinder in various flow regimes. *J. Fluid Mech.* **897**, A21.
- SRINIVASAN, S., CHOI, W., PARK, K.-C., CHHATRE, S.S., COHEN, R.E. & MCKINLEY, G.H. 2013 Drag reduction for viscous laminar flow on spray-coated non-wetting surfaces. *Soft Matt.* **9** (24), 5691–5702.
- SRINIVASAN, S., KLEINGARTNER, J.A., GILBERT, J.B., COHEN, R.E., MILNE, A.J.B. & MCKINLEY, G.H. 2015 Sustainable drag reduction in turbulent Taylor–Couette flows by depositing sprayable superhydrophobic surfaces. *Phys. Rev. Lett.* **114** (1), 014501.
- TAYLOR, G.I. 1923 Experiments on the motion of solid bodies in rotating fluids. *Proc. R. Soc. Lond. A* **104**, 213–218.
- THIELICKE, W. & SONNTAG, R. 2021 Particle image velocimetry for MATLAB: accuracy and enhanced algorithms in PIVlab. *J. Open Res. Softw.* **9** (1), 12.
- TRETHEWAY, D.C. & MEINHART, C.D. 2002 Apparent fluid slip at hydrophobic microchannel walls. *Phys. Fluids* **14** (3), L9–L12.
- TÜRK, S., DASCHIEL, G., STROH, A., HASEGAWA, Y. & FROHNAPFEL, B. 2014 Turbulent flow over superhydrophobic surfaces with streamwise grooves. *J. Fluid Mech.* **747**, 186–217.
- VERZICCO, R. & ORLANDI, P. 1996 A finite-difference scheme for three-dimensional incompressible flows in cylindrical coordinates. *J. Comput. Phys.* **123** (2), 402–414.
- WANG, D., *et al.* 2020 Design of robust superhydrophobic surfaces. *Nature* **582** (7810), 55–59.
- WANG, P., CHEN, M., HAN, H., FAN, X., LIU, Q. & WANG, J. 2016 Transparent and abrasion-resistant superhydrophobic coating with robust self-cleaning function in either air or oil. *J. Mater. Chem. A* **4** (20), 7869–7874.
- WATANABE, K., UDAGAWA, Y. & UDAGAWA, H. 1999 Drag reduction of Newtonian fluid in a circular pipe with a highly water-repellent wall. *J. Fluid Mech.* **381**, 225–238.
- WEN, J., ZHANG, W.-Y., REN, L.-Z., BAO, L.-Y., DINI, D., XI, H.-D. & HU, H.-B. 2020 Controlling the number of vortices and torque in Taylor–Couette flow. *J. Fluid Mech.* **901**, A30.
- WILLINGHAM, D., ANDERSON, W., CHRISTENSEN, K.T. & BARROS, J.M. 2014 Turbulent boundary layer flow over transverse aerodynamic roughness transitions: induced mixing and flow characterization. *Phys. Fluids* **26** (2), 025111.
- XUE, C.-H., GUO, X.-J., ZHANG, M.-M., MA, J.-Z. & JIA, S.-T. 2015 Fabrication of robust superhydrophobic surfaces by modification of chemically roughened fibers via thiol–ene click chemistry. *J. Mater. Chem. A* **3** (43), 21797–21804.
- ZHU, X., OSTILLA-MÓNICO, R., VERZICCO, R. & LOHSE, D. 2016 Direct numerical simulation of Taylor–Couette flow with grooved walls: torque scaling and flow structure. *J. Fluid Mech.* **794**, 746–774.